

Analysis of Traveling Waves in the Visual Cortex

Author: Michel Carroll (260584901)
August 11th, 2021

BIOL 466 – Independent Research Project
McGill University

Supervisor: Dr. Anmar Khadra (Department of Physiology)
Co-supervisor: Dr. Alanna Watt (Department of Biology)



Introduction

Travelling waves occurring in the extrastriate visual cortex have been implicated as a means of integrating motor and sensory signals.⁴ They can be detected in the primate brain following saccadic eye movements by measuring and fitting the local field potential (LFP)¹⁰ of the V4 visual cortex to a 2D sine wave. The strength and direction of these waves is most distinctive when the saccade is pointing towards the receptive field of the neurons (Figure 1). These travelling waves, caused by out-of-phase oscillations, are associated with a reorganization of the neuronal firing patterns. They are likely involved in prioritizing the processing of relevant information that must happen quickly in between saccades. However, the underlying mechanism behind these waves is not well understood.

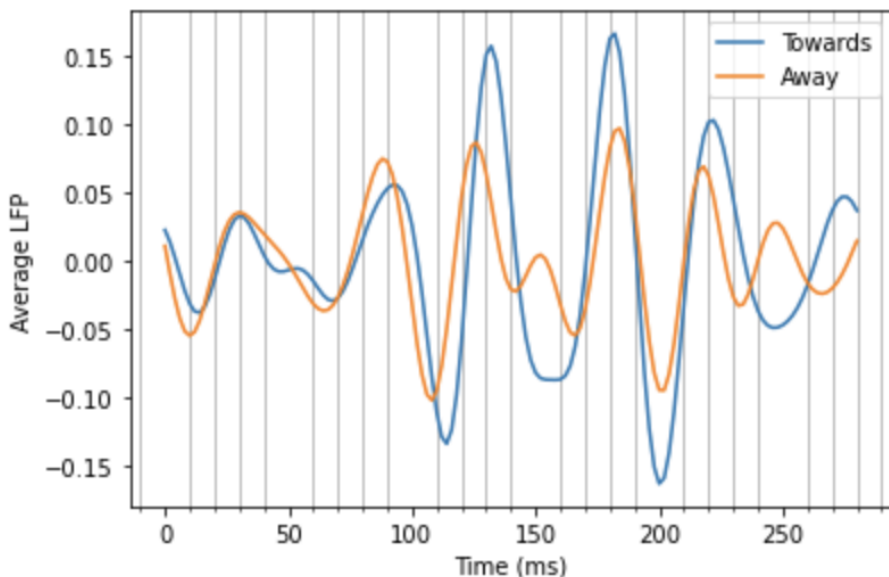


Figure 1: Average local field potential (LFP) across all sensors, grouped by the direction of the saccade.

We hypothesize that there exists other common spatiotemporal patterns in the context of saccades in the visual cortex, and that saccades towards and away from the target display different neurological patterns. The goal of this research project is to explore methods to detect and classify spatiotemporal patterns from the LFP recordings taken from the Zanos, T. et al. project.⁴ The full space of possible patterns are explored, not limited to travelling waves.

Manually inspecting the LFP data reveals a variety of different patterns besides travelling waves, including spirals, travelling bumps, and synchrony. Systematically identifying these patterns in the presence of noise is challenging. I explored the use of optical flow to parse

the spatiotemporal changes in the LFP and singular value decomposition (SVD) to identify and compare the dominant modes that recur in the recordings.³ I also consider the mean phase coherence of the LFP signals and how these evolve through the course of a recording.¹

Biological Context

The visual cortex is a structure in the brain responsible for processing visual information from the retina.⁹ The primary visual cortex, also known as the striate cortex, receives the input in raw form as color and illumination. The further interpretation of this information into higher level representations happens in the extrastriate layers of the brain. In primate brains, the V4 area of the visual cortex integrates input from the primary visual cortex and plays a role in object recognition.⁸

Saccadic eye movement is the sequential fixation of the eye on different targets with the goal of using the foveal of the retina on the most pertinent object. Multiple areas of the primate visual and motor areas of the brain must integrate together to perform saccades. In between saccades, the brain must quickly process the visual input from its target before starting the next saccade. Travelling waves in the V4 area are hypothesized to play a role in reorganizing the visual information across the visual space.⁴ While considering a specific area of V4, the amplitude of the wave is tuned to the direction of the saccade relative to the receptive field of that area, with a saccade towards the receptive field producing stronger and more directional waves than one saccades away from it.

Methods

Optical Flow Analysis

Optical flow is a video processing step which measures the apparent direction and amplitude of the movement of pixels in frames of a recording. The process takes as input a sequence of frames, and for each frame outputs a velocity vector field. In the context of neurobiology, optical flow is useful for combining both spatial and temporal information from neuronal recordings, and identifying distinct patterns of activity in either LFP or electroencephalogram (EEG) data.⁶

There are different algorithms for calculating optical flow, each with its own distinct properties. The one used in this project is the Horn-Schunck algorithm,⁶ a global method which iteratively minimizes a brightness and consistency constraint on the entire image field at once, producing a dense vector field (1). It stands in contrast to local methods such as Lucas-Kanade, which assume that nearby pixels exhibit the same motion and produce a sparse vector field. The Horn-Schunck algorithm is parametric; the α term is a required regularization term that controls the smoothness, with higher values placing more

weight on the consistency constraint. I chose a value of $\alpha = 1.0$ by trial and error, which produces a clean output for the LFP data.

$$\min_{u,v} \left\{ \int (I_t + I_x u + I_y v)^2 dx dy + \alpha \int (|\nabla u|^2 + |\nabla v|^2) dx dy \right\} \quad (1)$$

$I(x, y, t)$ is the intensity value of the pixels at each time point and space, while u and v are the components of each velocity vector in space.

The dominant spatiotemporal patterns can be identified from a recording by using singular-value decomposition (SVD).³ The first few modes contain the spatiotemporal patterns that display the most energy throughout the recording, and the remaining modes with less weight contain the less dominant patterns, including noise. To use SVD, the velocity vector field time series first needs to be represented as a two-dimensional matrix; this can be accomplished by representing each vector as a complex number, with its u component as the real component and the v component as the imaginary component. Once this transformation is applied, the input becomes a matrix with one row per sensor, and one column per time point. SVD decomposes the input into a product of 3 matrices: USV^T . The U matrix contains the dominant modes, the S matrix contains the variance explained by each mode, and the V^T matrix contains the time evolution of each mode.

Generating Patterns

To verify how well the optical flow and singular value decomposition methods performs, I used them against various artificial wave patterns. To generate a travelling wave, I used a 2D sine wave formula with added Gaussian noise. (2)

$$I(x, y, t) = \alpha \sin(xk_x + yk_y + tw) + \beta Z \quad Z \sim N(0, 1) \quad (2)$$

I generated a clean travelling wave with parameters $k_x = 0.1$, $k_y = 0.2$, $w = 0.5$, $\alpha = 0.25$, $\beta = 0$ in the time interval $t = [40, 80]$, immediately followed and preceded by a 40 frame period of quiescence. The result after applying optical flow and SVD is a travelling wave dominant mode that explains 60% of the variance (Figure A1). In the presence of noise ($\beta = 0.1$), the dominant mode still shows a travelling wave but it only explains 10.9% of the variance (Figure A2). Additionally, under noisy conditions, the non-dominant modes contain misleading patterns in the optical flow attributable to noise. Seeing if the time evolution of the modes averages to a non-zero value could be one way to filter out modes which are the product of noise in the data.

I generated spiral waves using (3) with $w = 0.25$ to see how well the method would generalize to other patterns (3).

$$I(x, y, t) = \alpha \sin\left(\tan^{-1}\left(\frac{y}{x}\right) + tw\right) + \beta Z \quad Z \sim N(0, 1) \quad (3)$$

The resulting dominant modes show less intuitive spatiotemporal patterns, however, the first two modes still explain a total of 87.2% of the variance in the recording (Figure A3). Due to the difficulty of interpreting these modes by manual inspection, this method for identifying spatiotemporal patterns could still be used to match dominant modes against a library of previously computed modes mapped to different patterns of interest.

When combining a recording with both a travelling wave and a spiral at distinct time periods (Figure A4), the second-most dominant mode shows a blend of the two patterns. This demonstrates that my method may not be suitable to isolate patterns from long-duration recording displaying different behaviours over time. Applying a sliding window to a long recording and calculating SVD on the smaller segments yields more interpretable results by allowing us to clearly identify patterns that only occur transiently, even in the presence of noise (Figure 2).

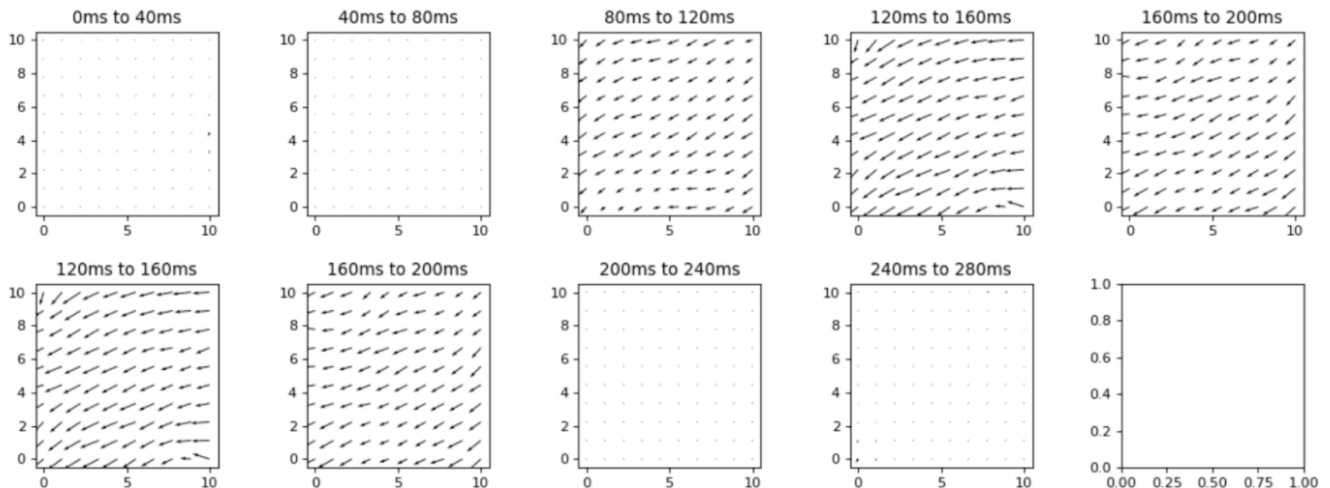


Figure 2: Dominant mode calculated on windows of 20 frames each from the noisy travelling wave pattern in Figure A2. Each frame corresponds to 2 milliseconds.

Classifying Patterns

I explored several ways of clustering the recordings based on their dominant modes. Classifying LFP recordings based on spatiotemporal similarities might allow us to associate particular behaviours to their relative positions within the recording. For example, clustering could help find a recurring pattern that immediately follows the end of the saccade. However, I wasn't able to find a reliable method of doing so.

To cluster recordings, a similarity metric between recordings must be developed. One difficulty that arises is if the orientation or exact location of the pattern is different, the velocity vector fields aren't easily comparable. Critical point analysis might offer some solutions to this problem.³ Characterizing the critical points present in the dominant modes would give a way to qualitatively compare patterns. The time evolution of modes could also be used to temporally correlate the occurrence of dominant modes between different recordings. Hierarchical clustering could then use the similarity metric to identify classes of patterns present in the data.

Assembling all the recordings together head-to-tail prior to running SVD against the "super-recording" could help identify recurring patterns that happen across many different recordings. However, this method would suffer from the fact that running SVD on a long recording containing many different patterns may result in blended modes (Figure A4). Also, computing SVD of a large matrix is a computationally intensive task, and may need to be run on specialized hardware for a sufficiently large amount of data.

Mean Phase Coherence Analysis

The level of coherence in the neurons over the recordings can be measured over different lengths of time. This can be estimated using the mean phase coherence (MPC)¹ between pairs of sensors over a sliding window of time, calculated as:

$$R = \left| \frac{1}{N} \sum_{j=0}^{N-1} e^{i\varphi} \right| , \quad \varphi = \phi_a(t) - \phi_b(t) \quad (4)$$

ϕ_a, ϕ_b represent the phase of the values from the pair of sensors. These can be found using the Hilbert transform after normalizing the sensors around their mean values during the window. This result is a value in the interval $R \in [0, 1]$ corresponding to the degree of coherence between the sensors. Calculating R over the cartesian product of all sensors results in a time series of MPC matrices showing snapshots of the coherence structure (Figure 3).

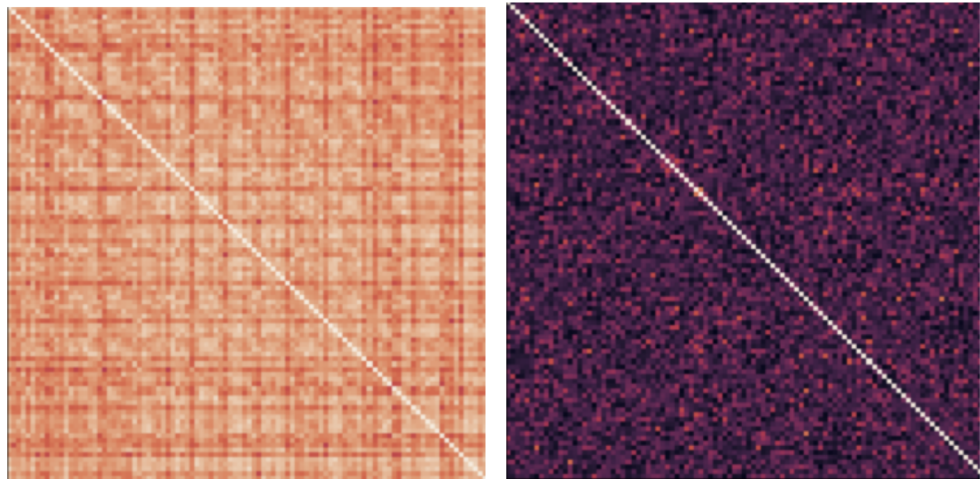


Figure 3: Mean phase coherence matrices for the noisy travelling wave in Figure A2. The figure on left is for the window $t \in [50, 80]$ and the right is for the window $t \in [0, 30]$. Lighter pixels represent higher R values.

To see how the coherence structure is changing through time, I plotted the distance between each pair of MPC matrix by calculating the mean difference between them (5). This allowed me to visualize the coherence structure dynamics at a glance.⁵ When done over all the different windows, the result is a distance matrix (Figure 4).

$$\zeta(t_1, t_2) \equiv \overline{|C_{ij}(t_1) - C_{ij}(t_2)|} \quad (5)$$

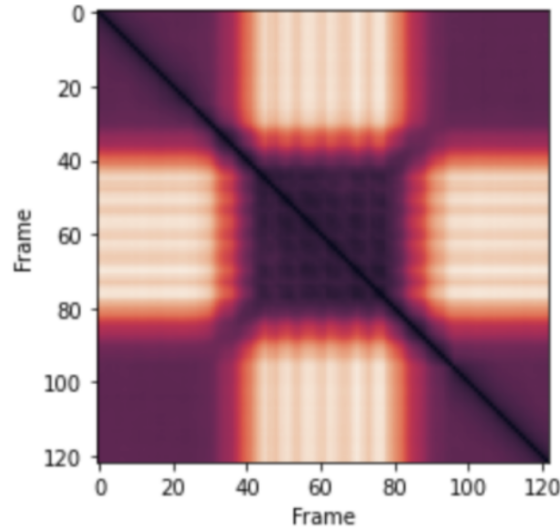


Figure 4: Distance matrix representing the mean phase coherence of the pattern in Figure A2. Lighter pixels represent shorter distances.

The resolution of the distance matrix depends on the size of the time window: a smaller window size displays a higher resolution (Figure 5).

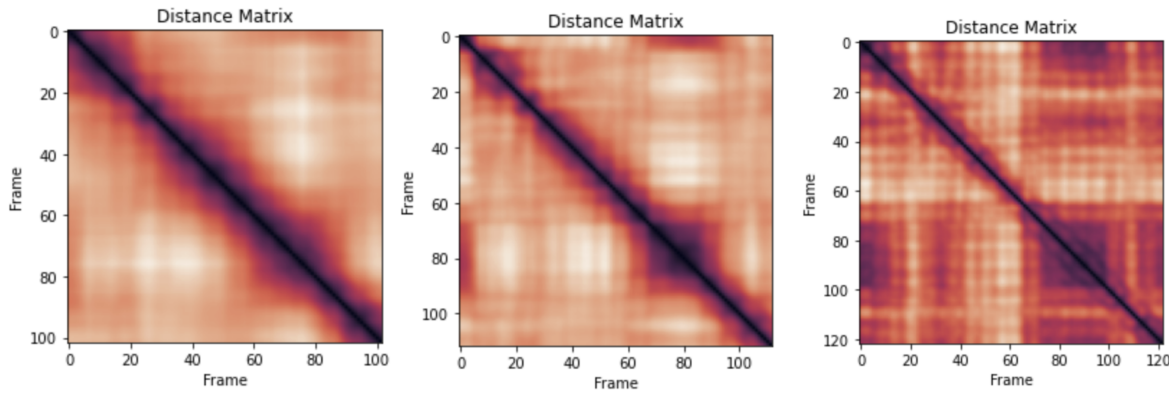


Figure 5: Distance matrices for one given LFP towards trial, calculated for a window length of 40 (left), 30 (center) and 20 (right).

To distinguish the different states from one another, the distance matrix can be ran against a clustering algorithm. I chose the Leiden algorithm, a graph-based clustering method based on the idea of finding well-connected communities while treating the distance matrix as an adjacency matrix.⁷ To do so, the distance matrix was transformed into a similarity matrix by taking the difference between the maximum value in the matrix. The result is a set of clusters associated to each window of time (Figure 6).



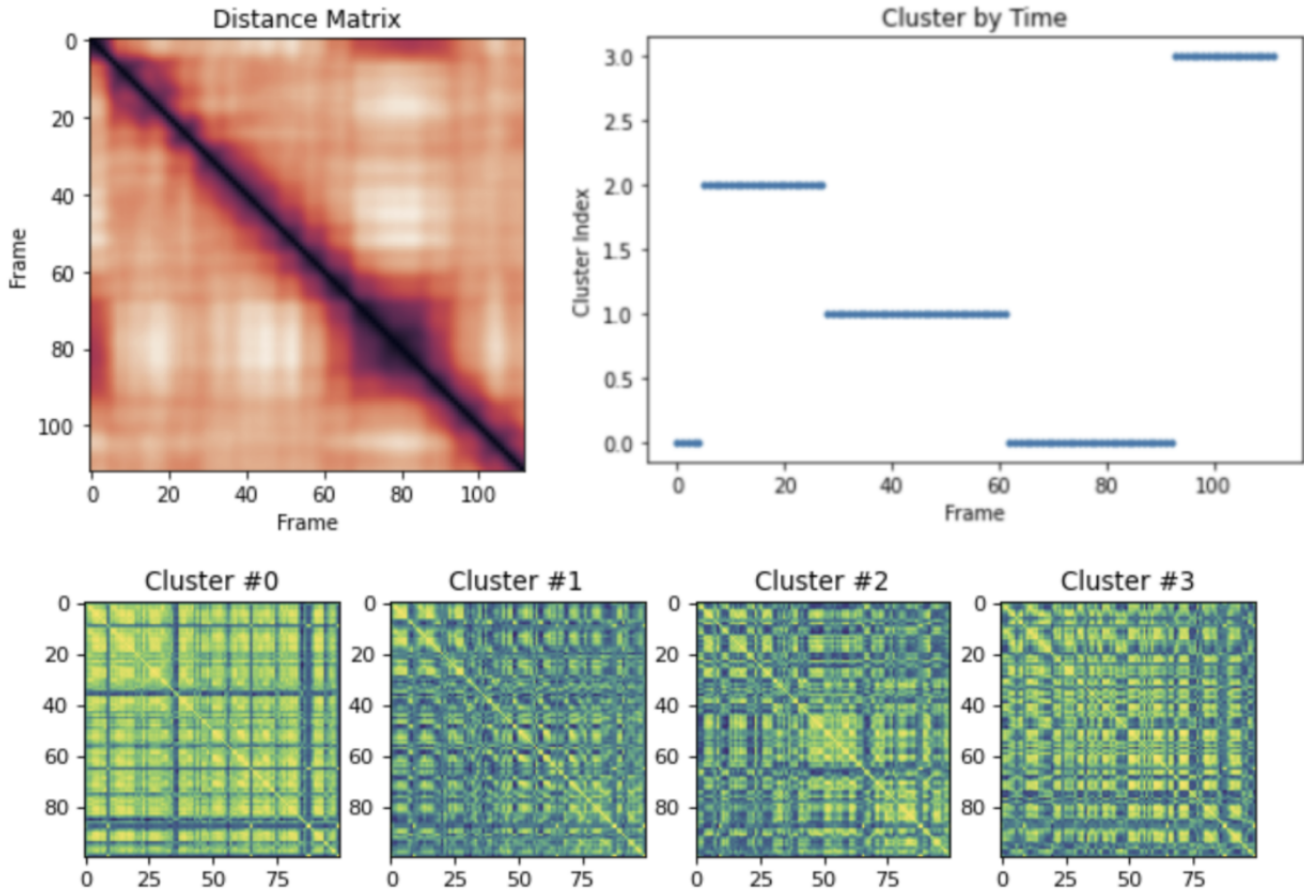


Figure 6: Representation of the different clusters in one of the towards trial recordings, using the Leiden algorithm. The bottom matrices are averages of all MPC matrices in the each cluster.

Calculating the distance matrix for all 2589 recordings in our dataset is a computationally heavy task, with the Hilbert transform step as the main bottleneck; on a MacBook Pro with a 2.2 GHz Intel Core i7 processor and 16GB of memory, one recording takes ~5 minutes. This task is easy to parallelize in a distributed cloud environment, since each recording is computed independently.

Software Tools

The analysis was completed in Python with support from several open-source scientific libraries: *numpy*¹¹, *scipy*¹² and *matplotlib*¹³. The *leidenalg*¹⁴ library was used to implement the Leiden clustering algorithm. *JupyterLab*¹⁵ was used as an interactive notebook environment to iterate quickly between coding and visualizing the results. Notebooks also helped make the results reproducible by keeping track of the steps in each analysis. A private GitHub repository was used as version control and a way to share code.

Distributing computational tasks across a cluster was necessary to run it in a parallel

manner. I used *Amazon Web Services*¹⁶ as cloud computing platform. To package the code so it could be run on the cloud, I built a Docker image to contain the analysis code and pushed it to AWS Elastic Container Registry. I saved the LFP input data into a private AWS S3 distributed object storage bucket for use by the Docker containers. AWS Batch was used to coordinate the parallel workload, whereby the output distance matrices were saved back into AWS S3. The output could then be downloaded back to visualize the output.

Results

Optical Flow Analysis

I investigated the ~~anatomy of the wave~~ after the end of the saccades by averaging all the independent trials together after grouping them by trial type, and then calculating the optical flow on the output. The output of the optical flow immediately following the end of the saccade can be observed using quiver plots. The direction of the wave in the towards trials (Figure 7) is apparent from the overall direction of the velocity field. By contrast, the wave in the away trials (Figure 8) is much more heterogeneous, with regions travelling in different directions.

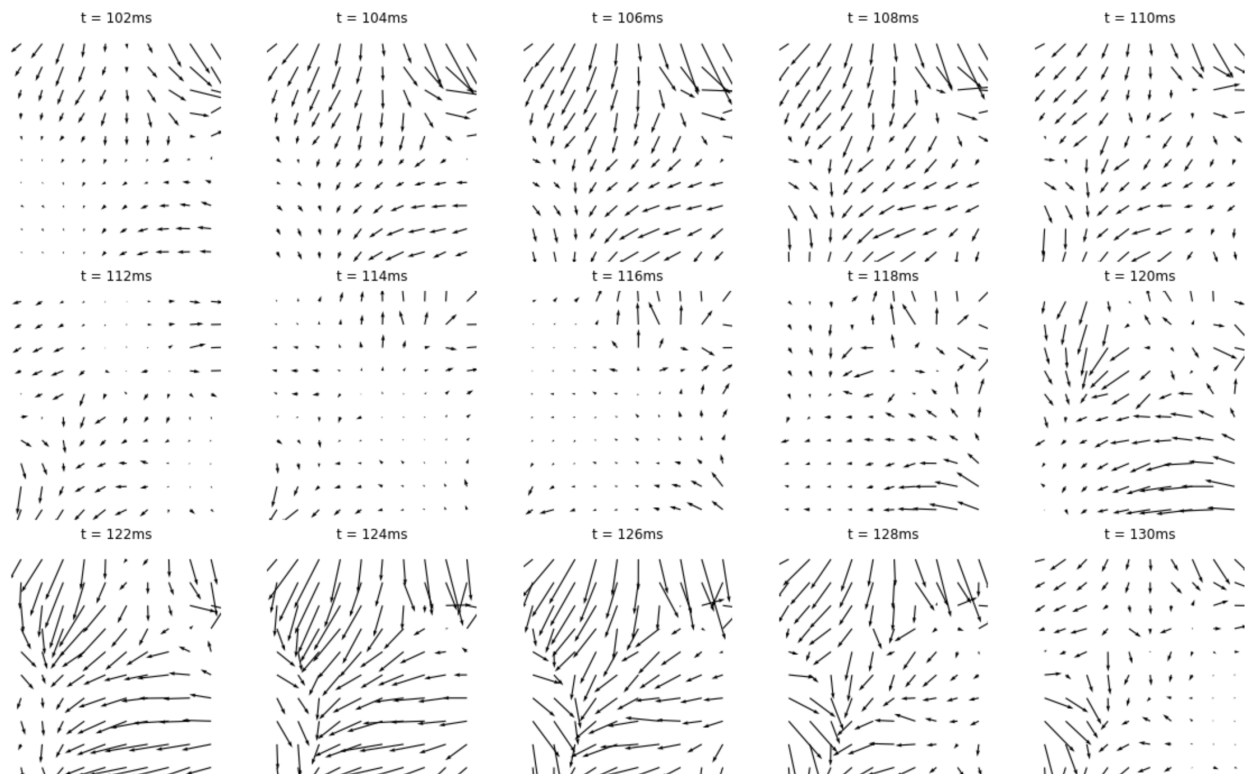


Figure 7: Mean optical flow time series of all averaged **towards trials** immediately following the end of the saccade.

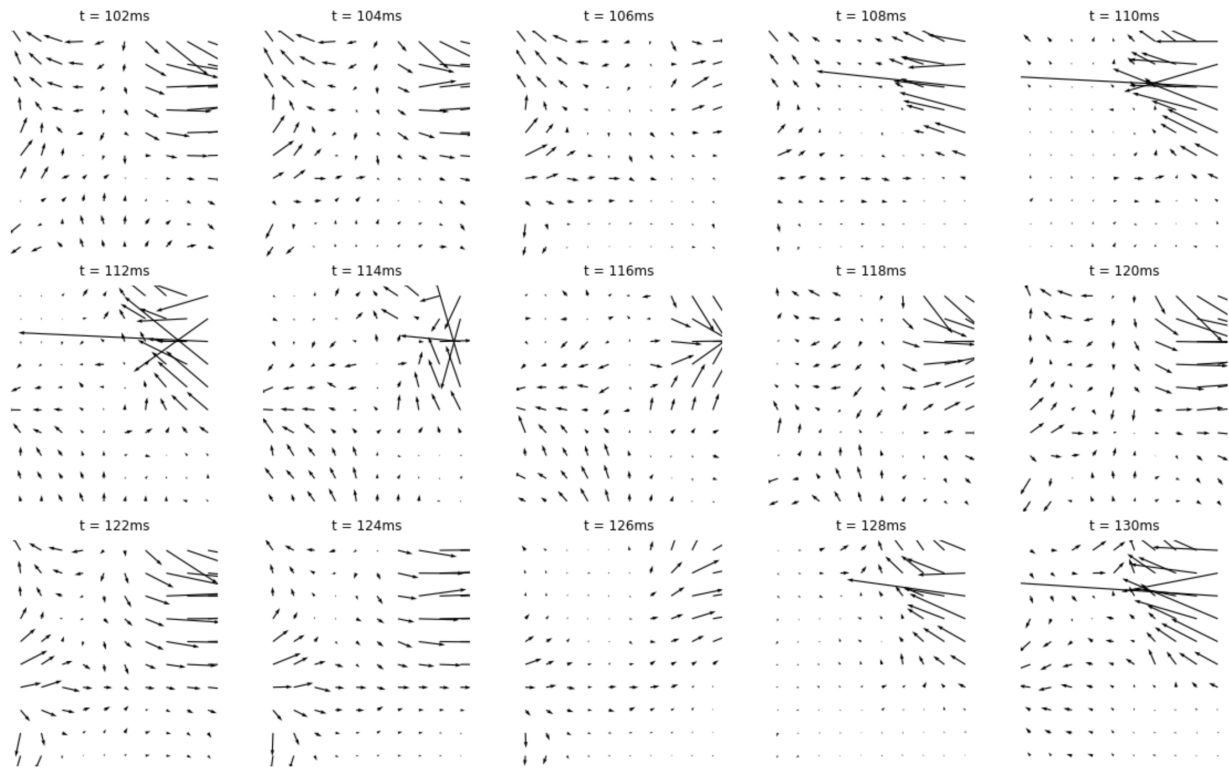


Figure 8: Mean optical flow time series of all averaged **away trials** immediately following the end of the saccade. The perturbations on the top-right corner of the plot is likely due to dead electrodes.

Mean Phase Coherence Analysis

Computing the MPC distance matrix of the recordings in our dataset yields a great variety of different coherence structures (Figure 9). Some show one or more clusters during which the coherence structure is relatively static (see top left matrix), while some show a more dynamic system without any distinctive states (see bottom left matrix).

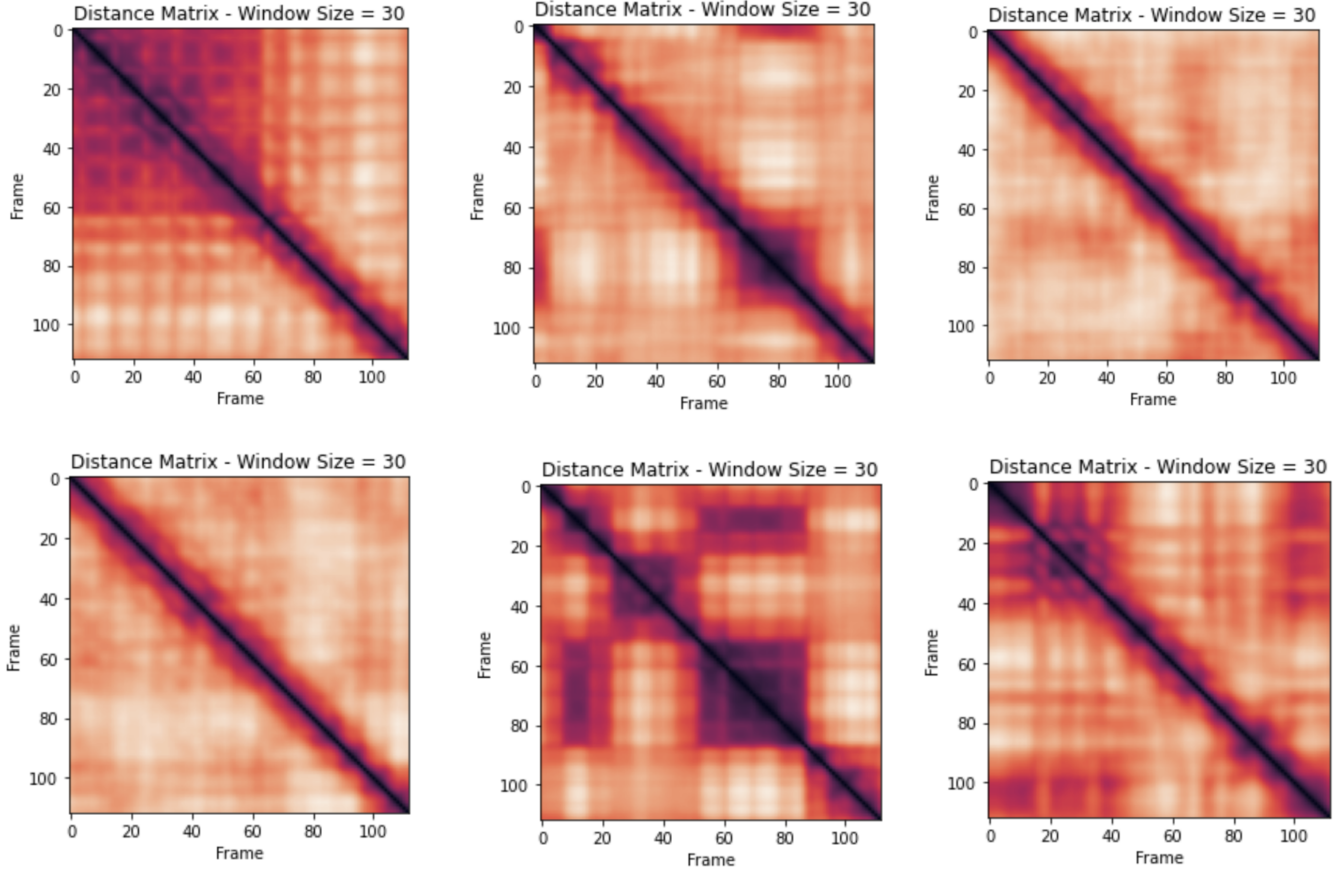


Figure 9: Distance matrices from a sample of different trials to demonstrate the many individual variations present in the dynamics of each recording. Lighter pixels correspond to a longer distance. Each timeframe corresponds to 2ms of recording time, and the MPC is calculated over 30 frame windows.

I averaged all the independent trials together after grouping them by category, and then calculated the mean phase coherence matrix of the output (Figure 10). While using a window length of 20 produces lots of artifacts and noise, both the window size of 30 and 40 converge on a common coherence structure unique between the towards and away trials.

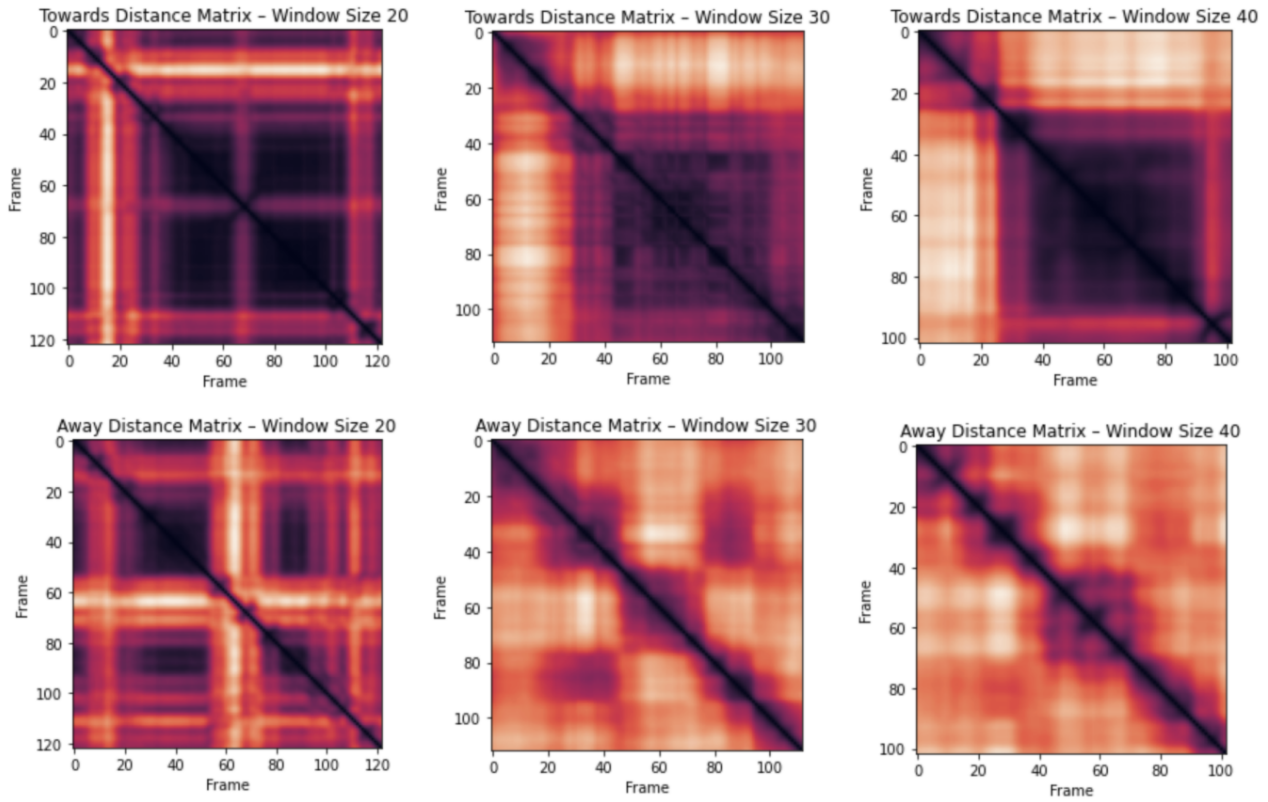


Figure 10: MPC distance matrices for the average of all recordings in each trial type, measured using window sizes of 20, 30 and 40 frames. Darker pixels represent **similar MPC structures**. Each timeframe corresponds to 2ms of recording time.

In the towards case, the coherence structure converges on a distinctive state after the 60-120ms window in the case of 30 frame windows, and 50-130ms in the case of 40 frame windows. Given that the end of the saccade occurs around the 100ms mark, this is evidence that the travelling wave has an effect on coherence. When applying the Leiden clustering algorithm to the distance matrix (Figure 11), we see that the mean phase coherence matrix prior to the end of the saccade shows low coherence (Cluster #1), while the cluster following it shows much greater coherence between all the sensors in the array (Cluster #0).

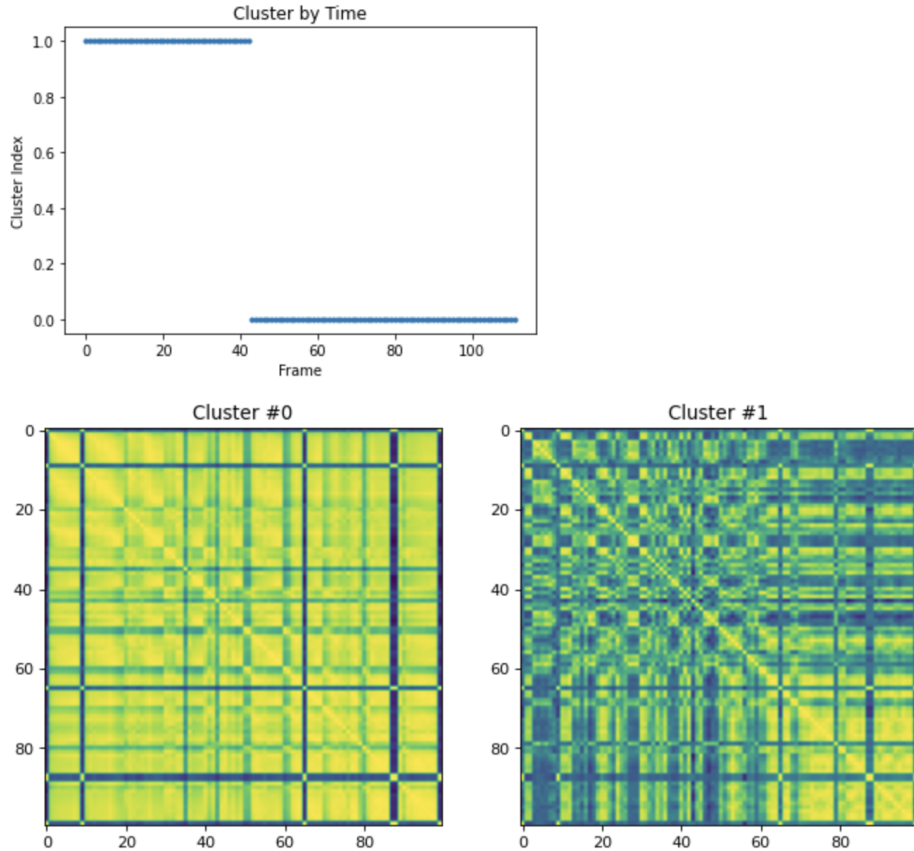


Figure 11: Clusters from the **towards trial** distance matrix with a window size of 30. Each timeframe corresponds to 2ms of recording time. Bottom matrices are the average of each cluster.

In the away case, the coherence structure forms four distinct clusters with one recurring twice during the recording (Figure 12). The coherence fluctuates between being high for a relatively short period of time after the end of the saccade (Cluster #0) to being low (Cluster #1). The coherence returns to an intermediate state at the end of the recording (Cluster #3).

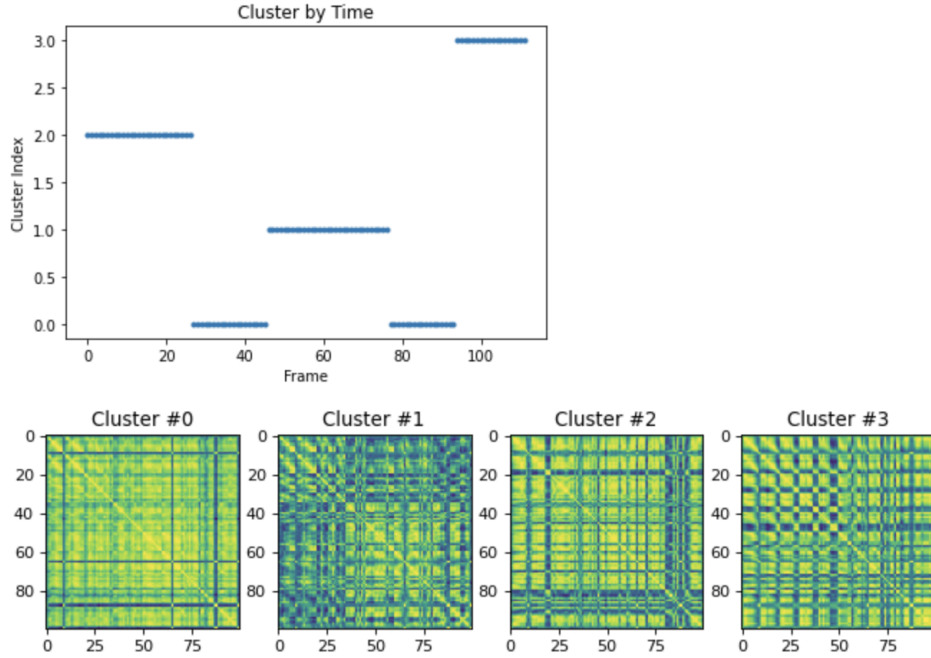


Figure 12: Clusters from the **away trial** distance matrix with a window size of 30. Each timeframe corresponds to 2ms of recording time. Bottom matrices are the average of each cluster.

Discussion

Travelling Wave Anatomy

The velocity vector field of the travelling wave following the end of the saccade agrees with some conclusions from the original paper.⁴ The wave observed after the towards trial generally has a greater amplitude and a more defined direction compared to the wave observed after the away trials. The optical flow analysis suggests that the wave has a more complex anatomy than a simple 2D sinusoidal wave, and that the wave travels at different speeds and directions in different regions of the visual cortex.

Averaging effects may occur when adding all the trials together; while the mean away trials field looks very heterogeneous (Figure 8), it may be due to the contribution of several wave types that occur independently. To gain more insight into what happens during individual saccades, clustering the trials based on the shape of the wave may help identify the different classes of behaviours. Singular value decomposition may be used to help clean up noise from the individual trials. Another way to validate would be to generate many noisy travelling waves that vary slightly in their orientation, averaging those together, calculating the optical flow and seeing if it results in a similar wave shape as in Figure 7 or Figure 8.

Investigating other optical flow algorithms more robust to noise might help interpret individual recordings with more confidence. The combined local-global optical flow method is a good candidate since it's less sensitive to local perturbations.¹⁰ The artifacts caused by the few dead electrodes in the array might be alleviated by it.

Coherence Structure

The mean phase coherence analysis results agree with the finding that the travelling wave towards the receptive field causes a postsaccadic phase reset.⁴ The high level of coherence following the saccade suggests that the preferred phase of the neurons occurs when they are in-phase with each other. The towards postsaccadic coherence structure is clearly distinct and stable, while for the away trials it's much less so. Having longer recordings before and after the saccade would help to validate if these clusters are in fact due to the saccade or simply other background effects.

Averaging all the recordings together might have had the effect of flattening out the oscillations from the data. If the baseline LFP are relatively incoherent and not tuned to any particular phase, summing the data points would cause destructive interference. Either running the mean phase coherence analysis on data from the fixation stage of the experiment, or generating artificial noisy out-of-phase LFP data and averaging it together, would help validate if this is the case or not.

To measure the degree to which the sensors are out-of-phase, we could introduce a τ term in the mean phase coherence equation (6). When the value is $\tau = 1$, this R value corresponds to the level of perfect synchronization between the sensors. The travelling wave is due to a phase differences between sensors. This difference can be calculated by finding the τ value which results in the highest R , interpretable as the delay until which the sensors become phase-locked. This would give us information on the speed of the travelling wave and its propagation through the array.

$$\max_{\tau} \left\{ R = \left| \frac{1}{N} \sum_{j=0}^{N-1} e^{i\varphi_j \tau} \right| \right\} \quad (6)$$



References

1. Mormann, F., Lehnertz, K., David, P., & E. Elger, C. (2000). Mean phase coherence as a measure for phase synchronization and its application to the EEG of epilepsy patients. *Physica D: Nonlinear Phenomena*, 144(3-4), 358-369. doi: 10.1016/s0167-2789(00)00087-7
2. Bruhn, A., Weickert, J., & Schnörr, C. (2005). Lucas/Kanade Meets Horn/Schunck: Combining Local and Global Optic Flow Methods. *International Journal Of Computer Vision*, 61(3), 1-21. doi: 10.1023/b:visi.0000045324.43199.43
3. Townsend, R., & Gong, P. (2018). Detection and analysis of spatiotemporal patterns in brain activity. *PLOS Computational Biology*, 14(12), e1006643. doi: 10.1371/journal.pcbi.1006643
4. Zanos, T., Mineault, P., Nasiotis, K., Guitton, D., & Pack, C. (2015). A Sensorimotor Role for Traveling Waves in Primate Visual Cortex. *Neuron*, 85(3), 615-627. doi: 10.1016/j.neuron.2014.12.043
5. Münnix, M., Shimada, T., Schäfer, R., Leyvraz, F., Seligman, T., Guhr, T., & Stanley, H. (2012). Identifying States of a Financial Market. *Scientific Reports*, 2(1). doi: 10.1038/srep00644
6. Afrashteh, N., Inayat, S., Mohsenvand, M., & Mohajerani, M. (2017). Optical-flow analysis toolbox for characterization of spatiotemporal dynamics in mesoscale optical imaging of brain activity. *Neuroimage*, 153, 58-74. doi: 10.1016/j.neuroimage.2017.03.034
7. Traag, V., Waltman, L., & van Eck, N. (2019). From Louvain to Leiden: guaranteeing well-connected communities. *Scientific Reports*, 9(1). doi: 10.1038/s41598-019-41695-z
8. Roe, A., Chelazzi, L., Connor, C., Conway, B., Fujita, I., & Gallant, J. et al. (2012). Toward a Unified Theory of Visual Area V4. *Neuron*, 74(1), 12-29. doi: 10.1016/j.neuron.2012.03.011
9. Jason M. Samonds, Nicholas J. Priebe, 1.22 - The Primary Visual Cortex, Editor(s): Bernd Fritzsch, *The Senses: A Comprehensive Reference* (Second Edition), Elsevier, 2020, Pages 392-412, ISBN 9780128054093, <https://doi.org/10.1016/B978-0-12-809324-5.24201-6>. (<https://www.sciencedirect.com/science/article/pii/B9780128093245242016>)
10. Destexhe, A., & Bedard, C. (n.d.). Local field potential. Scholarpedia. http://www.scholarpedia.org/article/Local_field_potential.
11. <https://numpy.org/>
12. <https://www.scipy.org/>
13. <https://matplotlib.org/>
14. <https://pypi.org/project/leidenalg/>
15. <https://jupyter.org>
16. <https://aws.amazon.com/>

Appendix

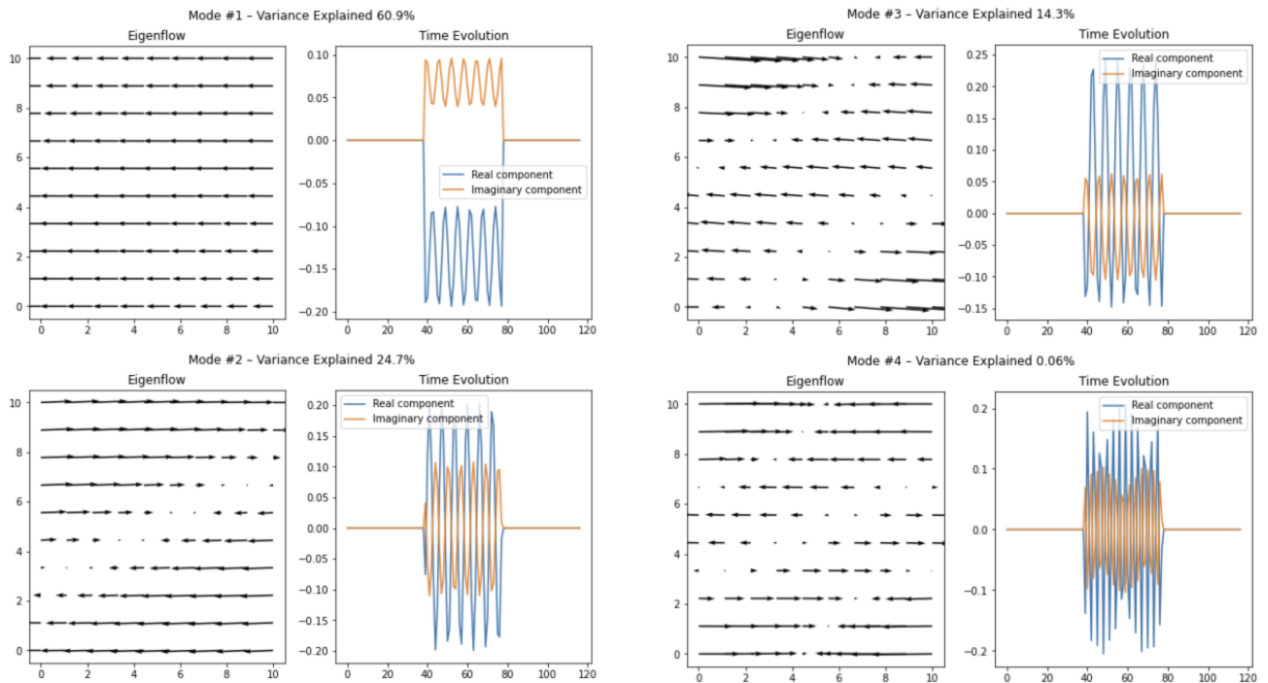
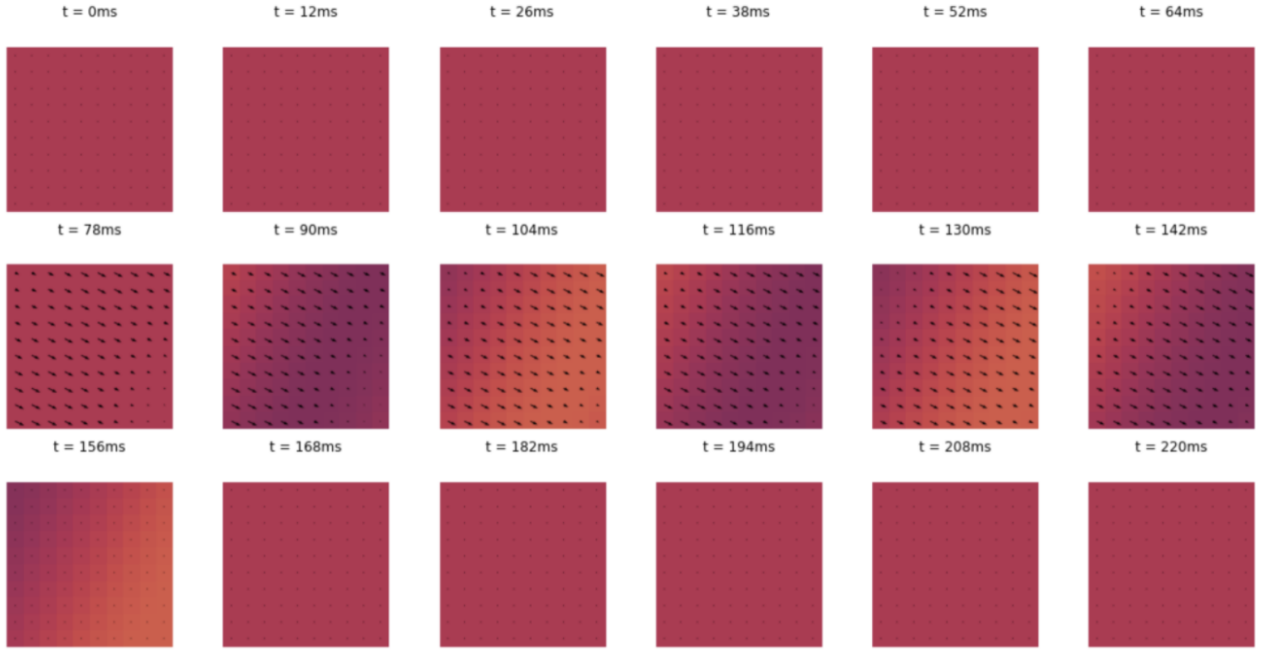


Figure A1: Horn-Schunk optical flow algorithm and SVD applied to travelling wave ($t \in [40, 80]$) with no noise

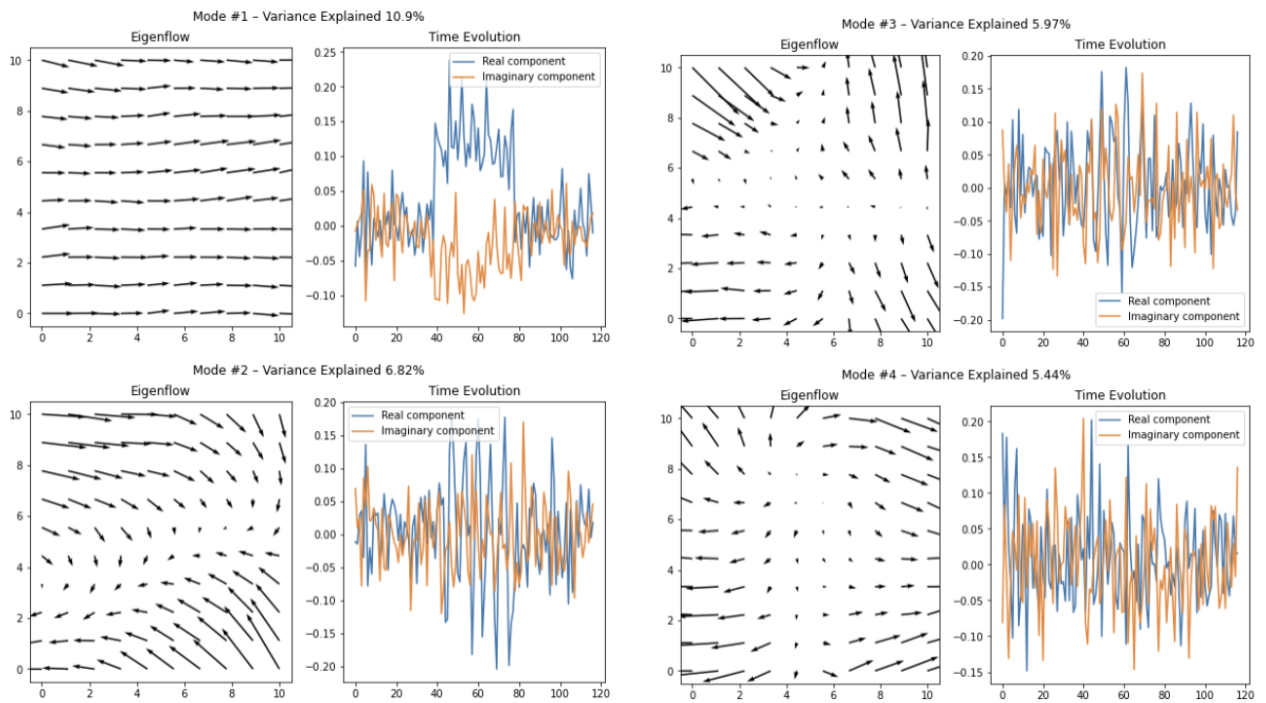
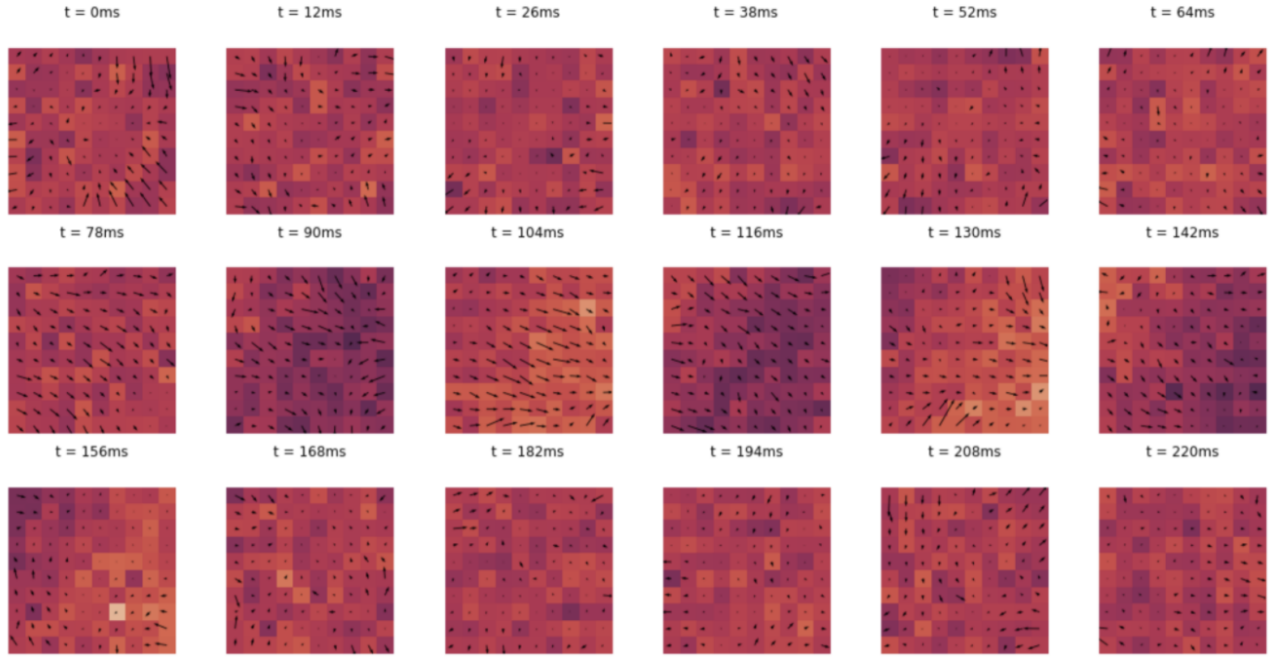


Figure A2: Horn-Schunk optical flow algorithm and SVD applied to travelling wave ($t \in [40, 80]$) with noise

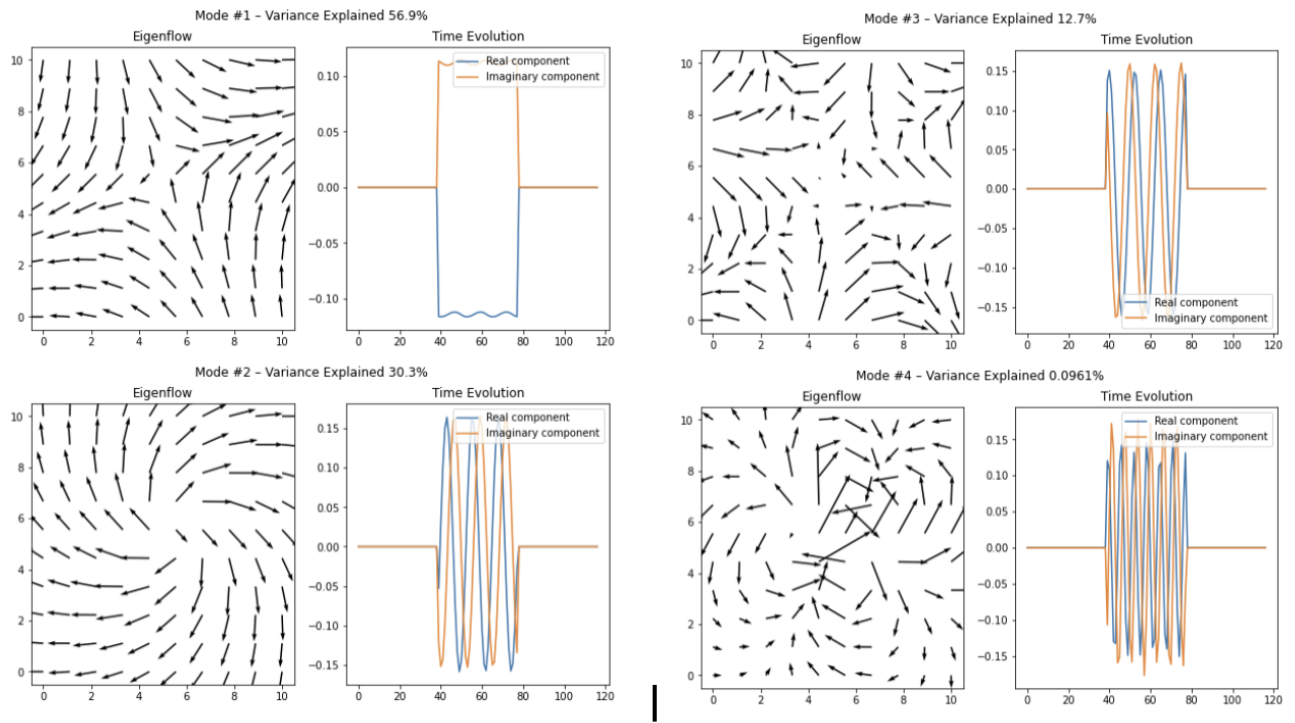
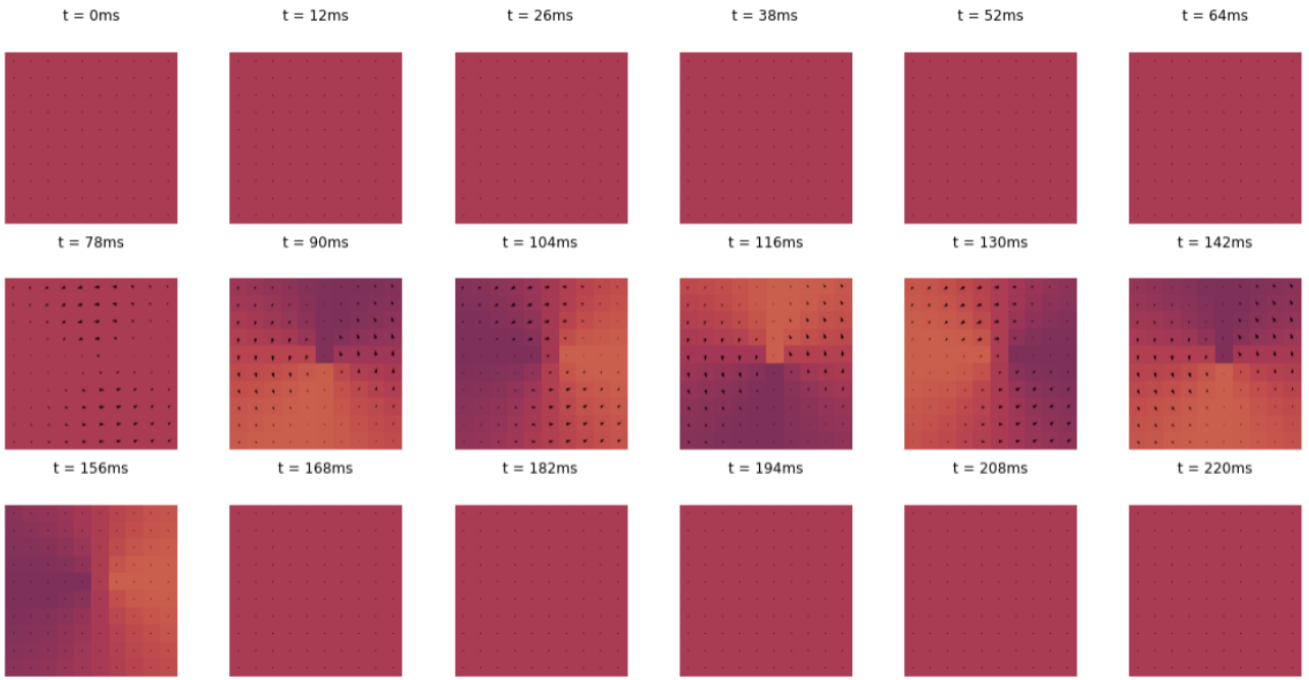


Figure A3: Horn-Schunk optical flow algorithm and SVD applied to spiral wave ($t \in [40, 80]$) with no noise

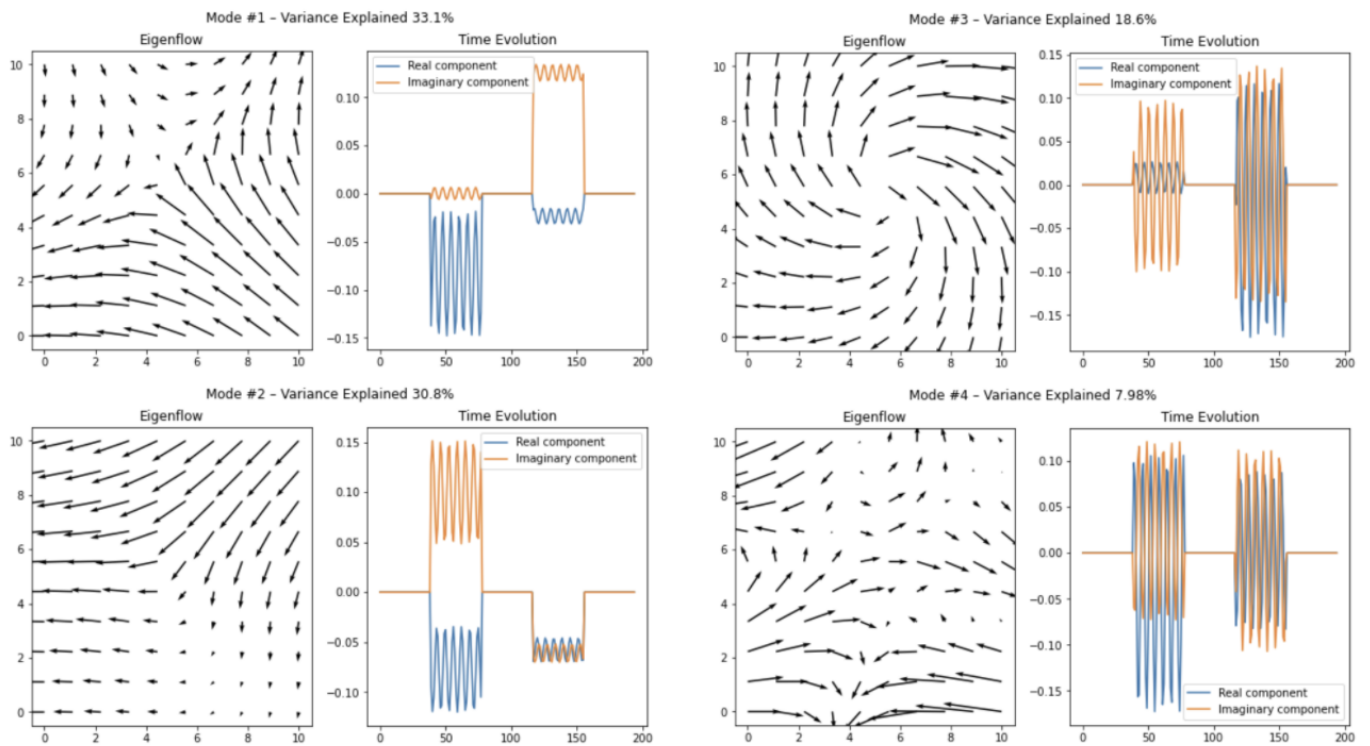
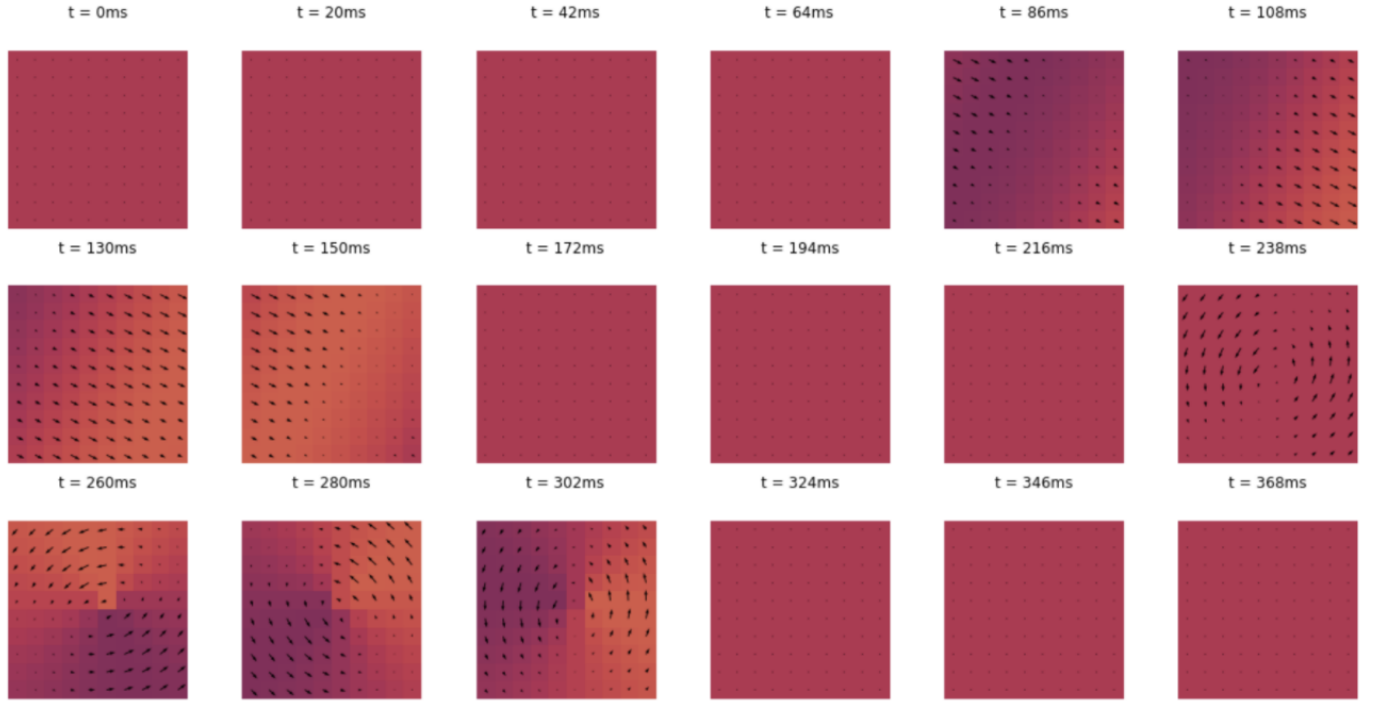


Figure A4: Horn-Schunk optical flow algorithm and SVD applied to a recording containing both a travelling wave $t \in [40, 80]$ and a spiral wave $t \in [120, 160]$